

EFFECTS OF DISTRIBUTED PROPELLER PLACEMENT ON LIFT ENHANCEMENT OF A HIGH-LIFT CONFIGURATION

Hui-Xian He[1,2], Wen-Ping Song[1,2,*], Yue Wang[1,2], Yi-Heng Wang[1,2] & Ya-Jun Shi[3]

[1] Institute of Aerodynamic and Multidisciplinary Design Optimization, School of Aeronautics, Northwestern Polytechnical University, Xi'an, Shaanxi 710072, People's Republic of China
[2] National Key Laboratory of Aircraft Configuration Design, Xi'an, Shaanxi 710072, People's Republic of China
[3] China Ship Scientific Research Center, Wuxi, Jiangsu 214082, People's Republic of China

Abstract

Slipstream-induced lift enhancement enabled by distributed electric propulsion (DEP) is one of the key approaches for improving the takeoff and landing performance of short takeoff and landing (STOL) aircraft. However, most existing studies have focused on propeller–wing interference in cruise configurations. For high-lift configurations with large flap deflections under takeoff conditions, the effects of propeller streamwise offset, vertical offset, and tilt angle on the lift characteristics require further investigation to fully exploit the potential of STOL aircraft for enhanced takeoff performance. In this study, a two-element high-lift system of a small eight-propeller distributed STOL aircraft is investigated. A momentum-source-based Reynolds-averaged Navier–Stokes (RANS) method is first used to examine the effects of three parameters on the lift characteristics, and high-fidelity Unsteady RANS (URANS) simulations of representative configurations are further performed to analyze the mechanisms of slipstream-induced lift enhancement. The momentum-source RANS results show that, as the vertical offset increases, the lift enhancement exhibits a 'decrease–increase–decrease' trend. The optimal lift enhancement is obtained when the vertical offset reaches 120% of the propeller radius, corresponding to a 54.1% increase relative to the baseline configuration without propellers. Under a fixed vertical offset, the influence of the streamwise offset on the lift enhancement is not significant. The optimal lift enhancement is achieved at a streamwise offset of 13.5% of the mean aerodynamic chord, while the lowest lift gain occurs at 4.5% of the mean aerodynamic chord, which still reaches 51.2% relative to the baseline configuration. When vertical offset and streamwise offset are fixed, increasing the tilt angle further enhances lift. The high-fidelity URANS results indicate that increasing the propeller vertical offset shifts the slipstream-affected region from the main wing toward the flap, thereby suppressing flow separation over the flap upper surface. Increasing the propeller streamwise offset intensifies the upper-surface suction peak over the main wing. Furthermore, increasing the propeller tilt angle increases the effective angle of attack of the wing, thereby further improving the lift characteristics.

Keywords: Short takeoff and landing (STOL) aircraft, Distributed propellers, Propeller layout, Slipstream, Lift enhancement

1. Introduction

Urban air mobility (UAM) is widely regarded as a promising solution for alleviating ground traffic congestion and improving travel efficiency in densely populated areas [1]. Compared with vertical takeoff and landing (VTOL) aircraft, short takeoff and landing (STOL) aircraft do not require prolonged hovering or purely vertical ascent and descent, thereby avoiding the high-power demand during hover and the associated penalties due to the propulsion system. Consequently, in recent years, STOL aircraft offer significant advantages in range, payload capability, and safety, which makes them a research focus in the UAM field [2]. Benefiting from the rapid development of electric propulsion technologies, STOL aircraft increasingly employ distributed electric propulsion (DEP) configurations. Such configurations arrange multiple propellers along the wing span to cover a large portion of the wing with slipstream, thus effectively improving the lift characteristics during takeoff, landing, and cruise [3].

https://doi.org/10.71945/icas2026_0516

The aerodynamic effects of propeller slipstream under cruise conditions have been extensively investigated. Cheng et al. [4] combined the vortex lattice method and actuator disk theory to systematically investigate the effect of propeller number on the aerodynamic characteristics of distributed-propulsion configurations. Seo et al. [5] examined the effects of propeller number, rotation direction, and inter-propeller spacing on wing lift and drag performance. Chen et al. [6] varied the angle of attack, propeller advance ratio, and propeller spacing to investigate isolated propeller–wing interference in distributed propeller arrays, and further analyzed the flow characteristics near the blade tips. Aref et al. [7] studied the influence of propeller rotation direction on the spanwise lift distribution of the wing and the role of blade pitch angle in regulating slipstream effects. Keller et al. [8] used a momentum source method to examine the effects of propeller thrust distribution and wing scale on propulsive efficiency under cruise conditions. Cao et al. [9] compared the effects of relative propeller position and rotation direction on slipstream behavior. These studies demonstrate that propeller slipstream can effectively improve wing lift enhancement, and that the effect depends on multiple parameters, including installation position, propeller number, advance ratio, rotation direction, and propeller spacing. However, these works mainly focused on cruise configurations and did not address slipstream-induced lift enhancement for wing–flap configurations during takeoff and landing.

Compared with cruise conditions, STOL aircraft are subject to more stringent lift requirements during takeoff and landing. These flight conditions involve larger angles of attack and flap deflection, which introduce strong adverse pressure gradients and complex separated flows. As a result, the interference mechanisms between the slipstream and the wing–flap configuration substantially differ from those in cruise configurations. Therefore, several studies have been conducted to investigate slipstream-induced lift enhancement under takeoff and landing conditions. Keller et al. [10] performed numerical simulations of a propeller-driven transport aircraft under landing conditions and investigated the effects of propeller number on the maximum lift coefficient. Beckers et al. [11] used a 2.5D CFD approach to study the influence of propeller installation position and tilt angle on an infinite-span wing with an infinite propeller array under initial-climb conditions. Li et al. [12] compared the slipstream-induced lift enhancement of different distributed-propulsion aerodynamic designs with a double-slotted flap configuration. Agrawal et al. [13] experimentally investigated the effects of spanwise-uniform propeller rotational speed and installation angle on the aerodynamic characteristics of distributed propulsion systems. Fei et al. [14] conducted low-speed wind-tunnel tests of the NASA high-lift propeller system, examining the effects of propeller installation height, diameter, and wing–flap deflection angle on lift enhancement.

In summary, although wind-tunnel experiments have provided preliminary insight into the effects of several propeller-position parameters on the lift enhancement characteristics of wing–flap configurations, there remains a lack of numerical studies that systematically reveal the effects of key propeller-layout parameters, including propeller vertical offset, streamwise offset and tilt angle. More importantly, under large flap-deflection conditions, the coupling mechanism between the propeller slipstream and flap-separated flow remains unclear, and detailed flow-field analyses are still insufficient. This limitation hinders a deeper understanding of slipstream-induced lift enhancement during takeoff and landing, and limits the exploitation of lift-enhancement potential of distributed STOL aircraft.

The remainder of this paper is organized as follows. Section 2 introduces the numerical methods used in this study and validates their accuracy using a benchmark case. Section 3 presents the propeller–wing–flap configuration investigated in this work, and examines the effects of propeller streamwise offset, vertical offset, and tilt angle on the lift enhancement using a momentum source method. Section 4 employs high-fidelity URANS computations to reveal the mechanisms of lift enhancement. The conclusions and outlook are presented in Section 5.

2. Numerical Methods and Validation

2.1 Numerical Methods

The three-dimensional compressible Reynolds-averaged Navier–Stokes (RANS) equations are discretized and solved using the finite-volume method. The integral form of the governing equations

in an inertial coordinate system can be written as

$$\frac{\partial}{\partial t}\iiint_V \mathbf{Q}\,dV + \iint_{\partial\Omega} \mathbf{F}\bullet\mathbf{n}\,dS - \iint_{\partial\Omega} \mathbf{F}_v\bullet\mathbf{n}\,dS = 0 \tag{1}$$

where Ω denotes the control volume, $\partial\Omega$ is the boundary of the control volume, $\boldsymbol{Q}$ is the vector of conservative flow variables, and $\boldsymbol{F}$ and $\boldsymbol{F_v}$ are the inviscid and viscous flux vectors, respectively. The corresponding physical quantities are defined as

$$\mathbf{Q}=\begin{bmatrix}\rho\\ \rho u\\ \rho v\\ \rho w\\ \rho E\end{bmatrix}\quad \mathbf{F}=\begin{bmatrix}\rho(\mathbf{q}-\mathbf{q}_b)\\ \rho u(\mathbf{q}-\mathbf{q}_b)+p\mathbf{I}_x\\ \rho v(\mathbf{q}-\mathbf{q}_b)+p\mathbf{I}_y\\ \rho w(\mathbf{q}-\mathbf{q}_b)+p\mathbf{I}_z\\ \rho H(\mathbf{q}-\mathbf{q}_b)+p\mathbf{q}_b\end{bmatrix}\quad \mathbf{F}_v=\begin{bmatrix}0\\ \tau_{xx}\mathbf{I}_x+\tau_{xy}\mathbf{I}_y+\tau_{xz}\mathbf{I}_z\\ \tau_{xy}\mathbf{I}_x+\tau_{yy}\mathbf{I}_y+\tau_{yz}\mathbf{I}_z\\ \tau_{xz}\mathbf{I}_x+\tau_{yz}\mathbf{I}_y+\tau_{zz}\mathbf{I}_z\\ \lambda_x\mathbf{I}_x+\lambda_y\mathbf{I}_y+\lambda_z\mathbf{I}_z\end{bmatrix}$$

Here, ρ, p, and E denote the density, pressure, and total energy per unit mass of the gas. The variables u, v, and w represent the velocity components in the x, y, and z directions. $\mathbf{q}=(u,v,w)^T$ is the flow velocity vector, and $\mathbf{q}_b = u_b\mathbf{I}_x + v_b\mathbf{I}_y + w_b\mathbf{I}_z$, where $\mathbf{I}_x$, $\mathbf{I}_y$, and $\mathbf{I}_z$ are the unit vectors of the Cartesian coordinate system. The turbulence model employed in the present computations is the one-equation Spalart–Allmaras (S–A) model [15]. Widely applied in numerical investigations of low-speed aircraft flow and propeller slipstream, this model features excellent robustness and computational precision. Its general form is expressed as

$$\frac{\partial\tilde{\nu}}{\partial t}+u_j\frac{\partial\tilde{\nu}}{\partial x_j}=c_{b1}(1-f_{t2})\hat{S}\tilde{\nu}-\left(c_{w1}f_w-\frac{c_{b1}}{\kappa}f_{t2}\right)\left(\frac{\tilde{\nu}}{d}\right)^2+\frac{1}{\sigma}\left\{\frac{1}{\partial x_j}\left[(\nu+\tilde{\nu})\right]\frac{\partial\tilde{\nu}}{\partial x_j}+c_{b1}\frac{\partial\tilde{\nu}}{\partial x_i}\frac{\partial\tilde{\nu}}{\partial x_i}\right\} \tag{2}$$

In the S–A model, the turbulent eddy viscosity μ_t is defined as

$$\mu_t=\rho\tilde{\nu}f_{v1} \tag{3}$$

where ν is the molecular kinematic viscosity, and f_{v1} is the near-wall damping function, which is given by

$$f_{v1}=\frac{\chi^3}{\chi^3+c_{v1}^3},\qquad \chi=\frac{\tilde{\nu}}{\nu} \tag{4}$$

The remaining parameters in the equation are defined as follows:

$$f_{t2}=c_{t2}exp(-c_{t4}\chi^2),\quad f_w=g\left(\frac{1+c_{w3}^6}{g^6+c_{w3}^6}\right)^{\frac{1}{6}}=\left(\frac{g^{-6}+c_{w3}^{-6}}{1+c_{w3}^{-6}}\right) \tag{5}$$

$$g=r+c_{w2}(r^6-r),\quad r=min\left[\frac{\tilde{\nu}}{\hat{S}\kappa^2d^2},10\right] \tag{6}$$

$$S=\Omega+\kappa\frac{\tilde{\nu}}{k^2d^2}f_{v2},\ \Omega=\sqrt{2W_{ij}W_{ij}} \tag{7}$$

$$W_{ij}=\frac{1}{2}\left(\frac{\partial u_i}{\partial x_j}-\frac{\partial u_j}{\partial x_i}\right),\quad f_{v2}=1-\frac{\chi}{1+\chi f_{v1}} \tag{8}$$

Two propeller models are employed in this study: a momentum source model and a blade-resolved propeller model. The steady momentum source model is computationally efficient and is therefore used for parametric survey. In contrast, the blade-resolved propeller model is simulated using the unsteady Reynolds-averaged Navier–Stokes (URANS) method, which provides higher fidelity and is used for detailed flow-field analysis of representative configurations.

In the momentum source model [16], the propeller thrust is uniformly distributed over a virtual disk in the form of a body force. The pressure difference across the disk accelerates the flow, while the torque exerted by the fluid is used to transfer angular momentum to the flow passing through the disk. The momentum source model has a significant advantage in computational efficiency, and is suitable for investigating the influence of design parameters. To model the actual propeller load distribution, Goldstein's optimum distribution assumption [17] is adopted. Accordingly, the body force in the momentum source model varies in the radial direction, and its radial distribution is expressed as

$$f_{bx} = A_x r^* \sqrt{1-r^*} \tag{9}$$

$$f_{b\theta} = A_\theta \frac{r^* \sqrt{1-r^*}}{r^*\left(1-r'_h\right)+r'_h} \tag{10}$$

Here, f_{bx} is the axial body-force component, $f_{b\theta}$ is the tangential body-force component, and r denotes the radial coordinate. A_x and A_θ are constants related to the propeller thrust, torque, and disk thickness.

In this study, the sliding-mesh method is employed to simulate the rotational motion of the blade-resolved propeller for detailed flow-field analysis of representative configurations. To accurately capture the unsteady flow characteristics associated with propeller rotation, the URANS method is used to solve Eq. (1). As shown in Figure 1, the computational domain is divided into two subdomains: a stationary domain and a rotating domain. Relative motion exists between these two domains at their interface, and the flow-field information is transferred through interpolation at the interface, enabling a coupled solution between the stationary and rotating domains.

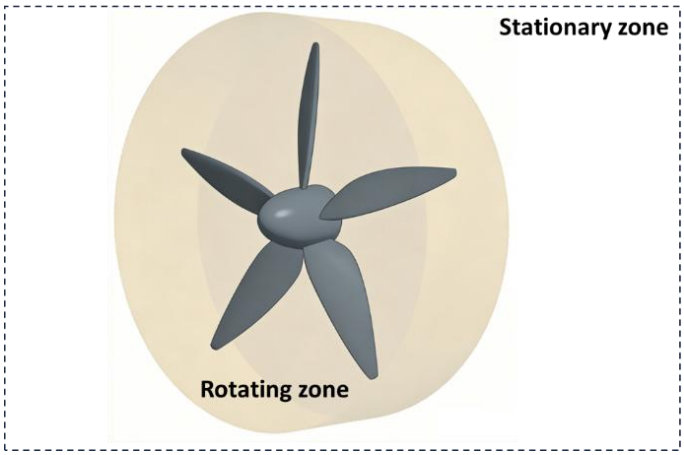
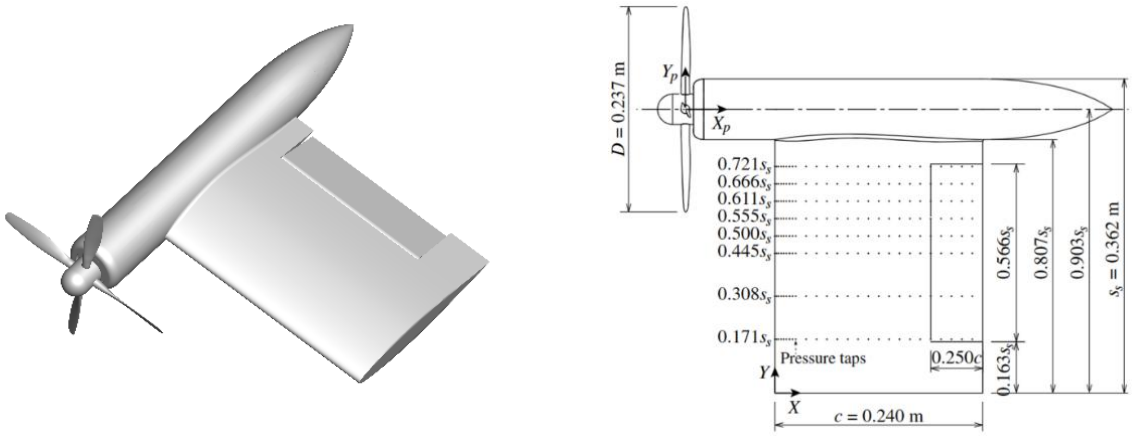


Figure 1 – Schematic of the computational domain division for the sliding-mesh method.

2.2 Validation

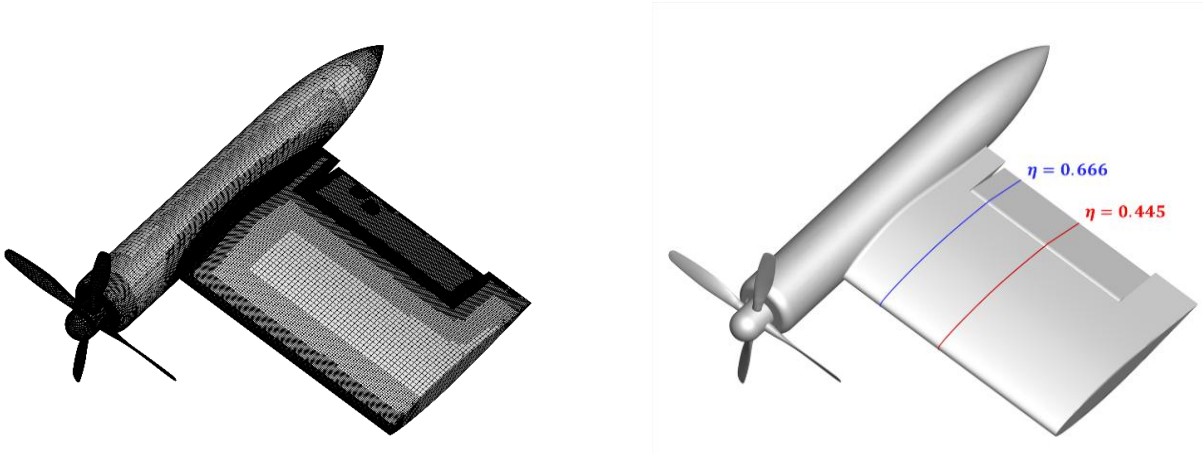
To validate the accuracy of the momentum source method and the URANS method used in this study for simulating propeller slipstream flows, a wingtip-mounted propeller benchmark case [18] is employed. Figure 2 shows the geometry and detailed parameters of the model. The propeller is a four-bladed propeller with a disk diameter of 0.237 m. Viewed from the wing trailing edge toward the leading edge; the propeller rotates clockwise. The wing uses a NACA 64(2) A015 airfoil and is equipped with a flap with a chord length equal to one quarter of the wing chord. The flap deflection angle is 10°.

The numerical simulation settings are kept consistent with those of the wind-tunnel test. The freestream velocity is 40 m/s, the angle of attack is 0°, the propeller rotational speed is 241.91 rps, and the Reynolds number based on the mean aerodynamic chord of the wing is 6.4×10^5. Figure 3(a) shows the surface mesh of the wingtip-mounted propeller model, and the total number of volume cells is approximately 20 million. Figure 3(b) shows two sectional locations inside and outside the propeller slipstream region, which are located at the spanwise stations of η=0.445 and η=0.666 respectively.



(a) Geometry schematic (b) Geometry parameters

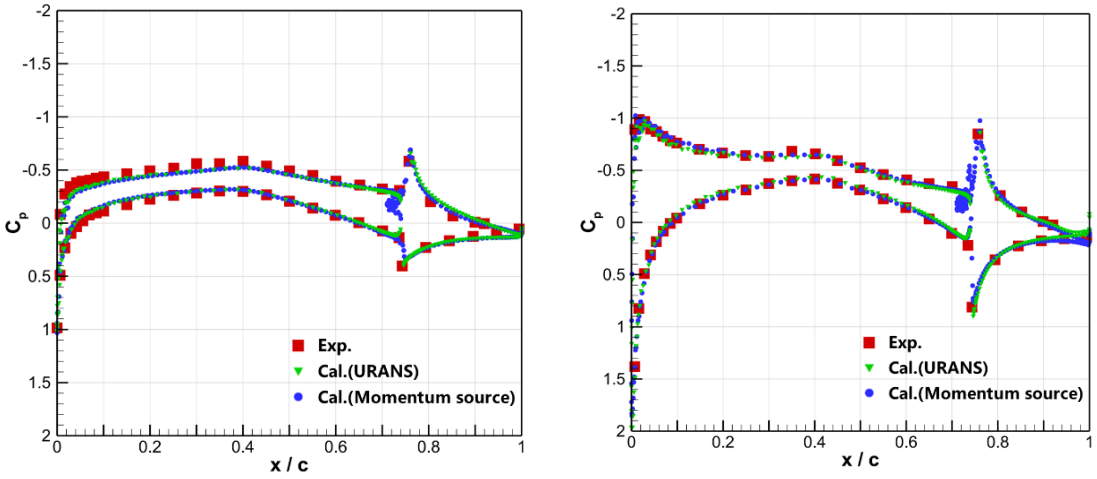
Figure 2 – Geometry of the wingtip-mounted propeller benchmark model [18].



(a) Surface mesh (b) The selected wing sections

Figure 3 – The selected wing sections and surface mesh of the CFD simulation.

Figure 4 (a) and (b) present the pressure distributions on the two wing sections computed using the URANS method and the momentum source method, together with the corresponding wind-tunnel measurements. The results show that the pressure distributions predicted by both methods agree well with the experimental data. Table 1 compares the lift coefficients of the benchmark model obtained using the momentum source method and the URANS method with the experimental value. The relative errors of the momentum source method and the URANS method are 2.86% and 0.49%, respectively.



(a) η=0.445 (b) η=0.666

Figure 4 – Comparison of computed and experimental pressure distributions.

Table 1 – Comparison of computed and experimental lift coefficients.

	Experiment	Momentum source	URANS
C_L	0.2657	0.2581	0.2670
Error	——	2.86%	0.49%

In summary, the momentum source method offers high computational efficiency, although its flow-field prediction accuracy is limited; the URANS method can resolve the unsteady effects induced by propeller blades with higher fidelity. Therefore, in this study, the momentum source method is used to investigate the effects of propeller vertical offset, streamwise offset and tilt angle. By rapidly computing the aerodynamic characteristics of configurations with different propeller-parameter combinations, this study analyzes the influence of each parameter on the lift enhancement of the high-lift configuration. On this basis, the URANS method is employed to perform detailed flow-field simulations of representative configurations, so as to further reveal the mechanisms of slipstream-induced lift enhancement under different propeller parameters.

3. Influence Patterns of Propeller Position on Lift Enhancement Via Momentum Source RANS Method

3.1 High-Lift Configuration

Figure 5 illustrates the distributed propeller-wing-flap high-lift configuration investigated in this study. The wing has a span of 4.8 m and a mean aerodynamic chord of 2.2 m. Since high lift is required during takeoff, the takeoff condition is selected as the representative operating condition. The freestream velocity is 90 km/h, and the angle of attack is 8°. Four five-bladed propellers are mounted on each side of the wing, with a spacing of 0.8 m between adjacent propellers. Each propeller has a radius of 0.33 m and rotates at 5500 rpm. The horizontal distance from the propeller disk center to the wing leading edge is defined as the streamwise offset X_P, and the vertical distance is defined as the vertical offset Z_P. The propeller tilt angle is denoted by θ. The streamwise offset X_P and vertical offset Z_P are defined as:

$$\begin{aligned} \mathrm{X_P} &= x_{leading} - x_{propeller} \\ \mathrm{Z_P} &= z_{leading} - z_{propeller} \end{aligned} \tag{11}$$

where $X_{propeller}$ and $Z_{propeller}$ are the horizontal and vertical coordinates of the propeller disk center, respectively. The $X_{leading}$ and $Z_{leading}$ are the corresponding coordinates of the wing leading-edge reference point. The streamwise offset X_P and vertical offset Z_P are expressed in terms of wing mean aerodynamic chord c and propeller radius R, i.e., X_P/c and Z_P/R.

Figure 5(b) presents three typical spanwise sections centered on the second propeller from the root of the wing, which are primarily used for subsequent flow mechanism analysis. Specifically, sections DV1 and DV3 are located at the spanwise stations of 50% propeller radius on the upwash side and downwash side of the propeller, respectively, while section DV2 coincides with the central axial plane of the propeller.

Figure 6 presents the computational mesh for the propeller-wing-flap configuration and its DV2 section. The entire flow domain is discretized with unstructured Cartesian grids, with body-fitted prism layer grids generated in the near-wall region. To meet the requirement of y^+=1, the height of the first wall-normal grid layer is controlled at 1.5×10^{-5} m. Local mesh refinement is applied to critical flow regions, including the wing leading and trailing edges, flap leading and trailing edges, and the flap slot. Following a grid convergence study, a mesh with approximately 49 million cells is finally selected for the subsequent numerical investigations.

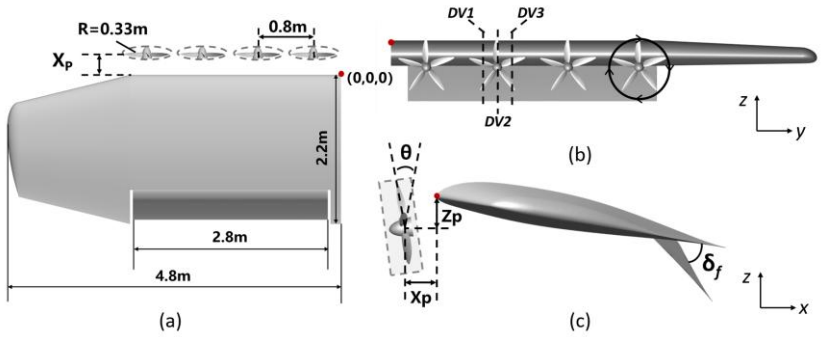
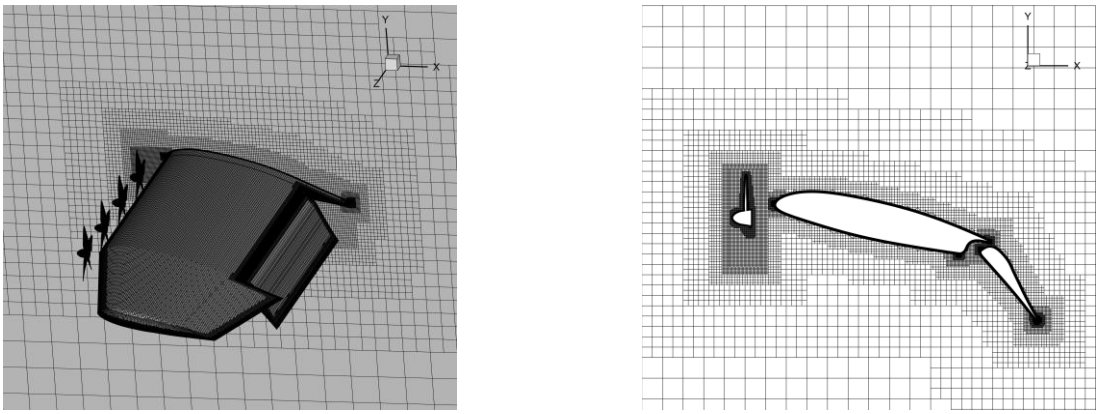


Figure 5 – Schematic diagram of the propeller-wing-flap configuration.



(a) Propeller-wing-flap configuration (b) DV2 section

Figure 6 – Computational mesh of the investigated configuration and the section DV2.

The parameter ranges for variable parameters are listed in Table 2. To improve the computational efficiency, the momentum source method is adopted to calculate the lift coefficients of configurations with various parameter combinations. In this method, the propeller is modeled as an actuator disk to simulate the aerodynamic-propulsive coupling effect between the propeller slipstream and the high-lift configuration.

Table 2 – Considered ranges for variable parameters.

Parameter	Lower limit	Upper limit	Step size
Streamwise offset X_P/c [%]	4.5	18	4.5
Vertical offset Z_P/R [%]	0	150	30
The propeller tilt angle θ [°]	2	24	2
Deflection angle of flap δ_f [°]	20	40	10

3.2 Influence Patterns of Propeller Position Parameters

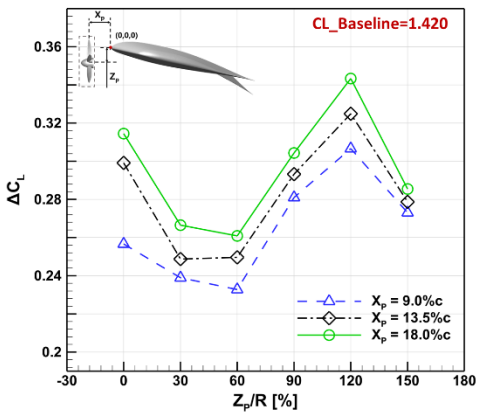
Figure 7 presents the variation of lift enhancement of the propeller-equipped high-lift configuration over the propeller-free baseline with the propeller vertical offset Z_P for various flap deflection angles, where $\Delta C_L = C_{L_prop} - C_{L_baseline}$ represents the lift difference between the propeller-integrated high-lift configuration and the propeller-free baseline configuration.

The results show that within the flap deflection range of 20° to 40°, the propeller-induced lift enhancement exhibits a non-monotonic variation pattern of ‘decrease–increase–decrease’ with increasing propeller vertical offset:

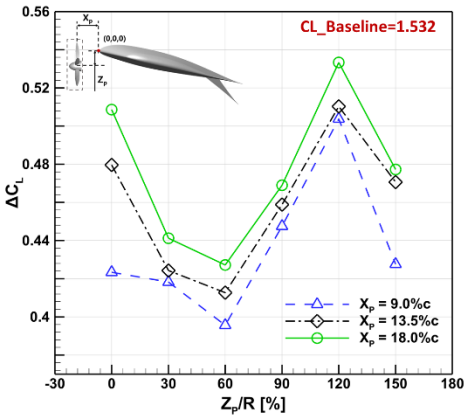
Local minima appear at vertical offsets of 30%R (20° and 30° flap deflection) and 60%R (40° flap deflection) relative to the wing leading edge. Thereafter, the lift enhancement rises continuously as the propeller vertical offset increases, and reaches the optimal value at Z_P=120%R.

The performance of overall lift enhancement is optimal at a flap deflection angle of 40°. Specifically, when the propeller is positioned at X_P=13.5%c and Z_P=120%R, the maximum lift enhancement is achieved: the lift coefficient increment is approximately 0.771, corresponding to a 54.06%

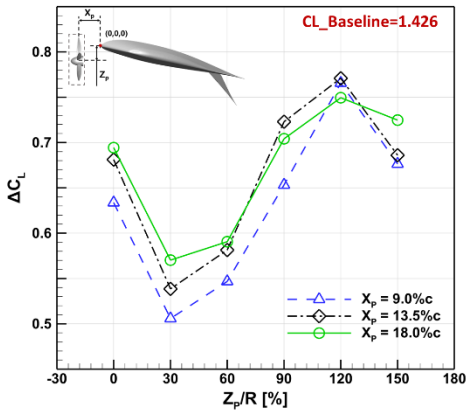
improvement over the propeller-free baseline configuration. In contrast, at the propeller position of X_P=9%c and Z_P=30%R, the lift enhancement of the high-lift configuration is the weakest under this flap deflection, with the lift coefficient increment amounting to 35.5% relative to the baseline.



(a) 20° flap deflection



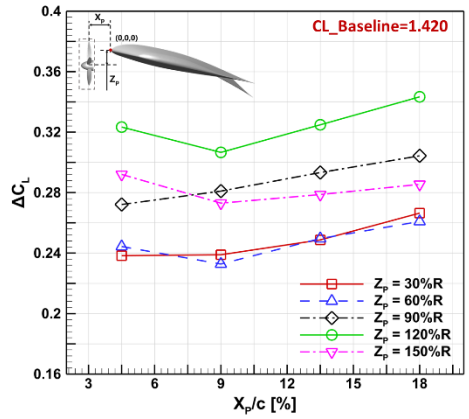
(b) 30° flap deflection



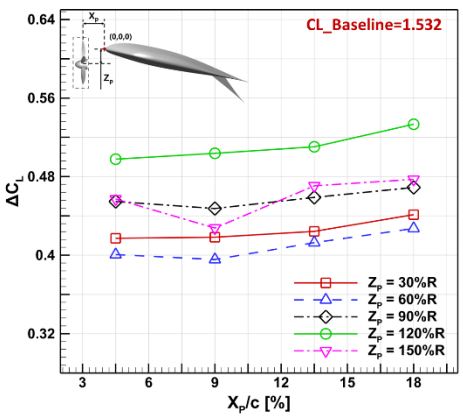
(c) 40° flap deflection

Figure 7 – Variation of lift coefficient increment with Z_P for various flap deflections.

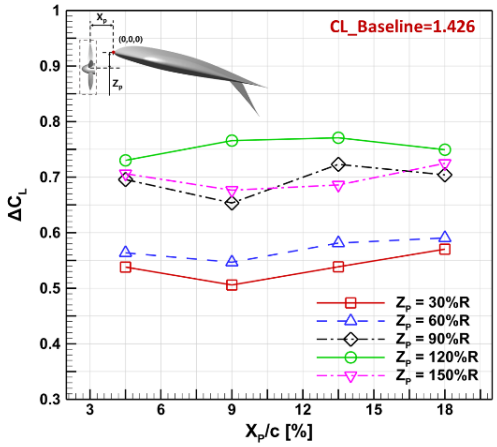
Figure 8 presents the variations of lift coefficient increment of the wing-flap configuration under propeller slipstream with streamwise propeller position X_P at flap deflections of 20° to 40°. Comparative analysis indicates that the lift increment varies weakly with streamwise offset at a fixed vertical offset. The maximum lift coefficient increment relative to the baseline configuration occurs at a flap deflection of 40° and a vertical offset Z_P=120%R. Under this condition, the optimal lift enhancement is achieved at a streamwise offset of 13.5%c, with the lift coefficient increment reaching 54.06% compared with the propeller-free baseline. By contrast, the minimum increment is 51.2%, at the streamwise offset of 4.5%c.



(a) 20° flap deflection



(b) 30° flap deflection



(c) 40° flap deflection

Figure 8 – Variation of lift coefficient increment with X_P for various flap deflections.

Figure 9 illustrates how the lift coefficient increment of the high-lift device varies with propeller tilt angle at different propeller positions. The increment increases with the tilt angle, and greater propeller vertical and streamwise offsets yield stronger lift enhancement.

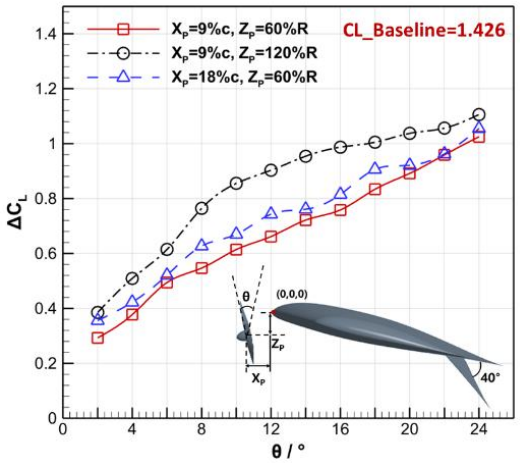
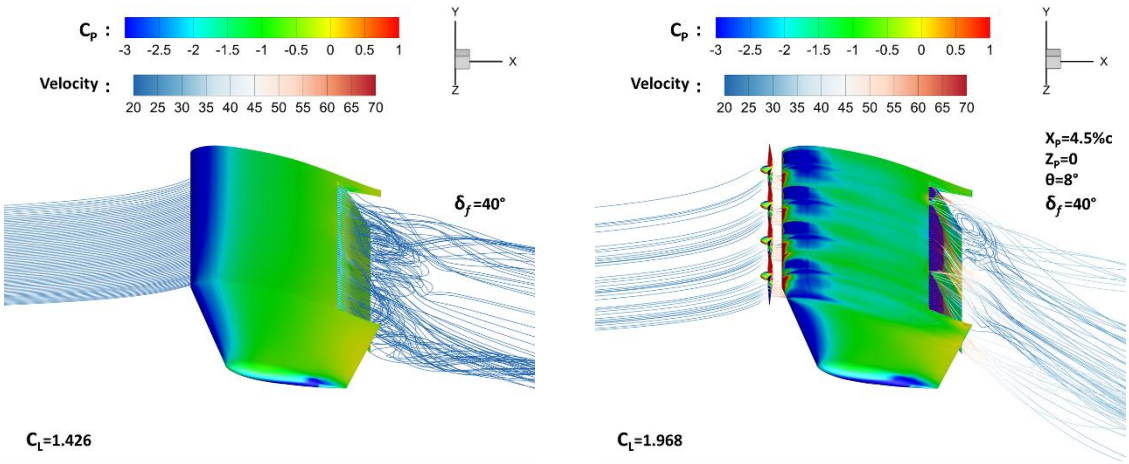


Figure 9 – Variation of lift coefficient increment with propeller tilt angle θ.

4. Lift-Enhancement Mechanisms Associated with Propeller Position Parameters Using High-Fidelity URANS

To further analyze the mechanisms of propeller position parameters on lift enhancement, this section adopts the high-fidelity URANS method for detailed flow field simulation of typical configurations.

Figure 10 compares the streamlines and surface pressure distributions between the baseline configuration and the propeller-equipped configuration at a flap deflection of 40°. The baseline configuration suffers from prominent large-scale flow separation. Severe adverse pressure gradients at the flap leading edge result in the flow separation and the formation of a large low-speed recirculation zone on the flap upper surface. Streamlines deviate significantly from the flap surface, so the high-lift capability of the whole flap cannot be realized. In contrast, the flow field is fundamentally improved after introducing distributed propeller slipstream. On the one hand, the slipstream accelerates the airflow over the upper wing surface, expands the low-pressure region and increases the pressure difference between the upper and lower wing surfaces. On the other hand, slipstream passes through the wing-flap gap and interacts directly with the separated flow on the flap surface. It injects momentum into the boundary layer and effectively mitigates the severe adverse pressure gradient on the flap surface. The originally separated flow reattaches to the surface, and the separation zone on the upper flap surface nearly disappears. Streamlines flow smoothly along the flap contour toward the trailing edge, resulting in a substantial lift enhancement.



(a) Baseline configuration (b) Propeller-equipped configuration

Figure 10 – Comparison of streamlines between baseline configuration and propeller-equipped configuration at a flap deflection of 40°.

The above comparison provides a preliminary understanding of the lift enhancement mechanism of propeller slipstream. The propeller position relative to leading edge of wing (X_P and Z_P), together with tilt angle, determines where the slipstream momentum is introduced and how effectively momentum is injected. To gain deeper insights into the mechanisms of different propeller layout parameters, we subsequently discuss the effects of vertical offset, streamwise offset and tilt angle on the high-lift configuration.

4.1 Lift-Enhancement Mechanism Associated with Propeller Vertical Offset

To examine the influence of vertical propeller position Z_P, flow field comparisons are conducted on typical configurations with varying vertical offsets. The evolution of lift enhancement is analyzed, with detailed propeller position parameters given in Table 3.

Table 3 – Typical configurations with varying vertical offsets.

Case	X_P/c	Z_P/R	θ
1	9%	0	8°
2	9%	30%	8°
3	9%	120%	8°
4	9%	150%	8°

Figure 11 compares the spanwise lift distribution of the wing between the baseline configuration and configurations with different propeller vertical offsets at a flap deflection of 40°. The results indicate that the propeller vertical offset plays a dominant role in lift enhancement performance and spanwise lift distribution. As the vertical offset increases, the lift enhancement presents a "decrease-increase-decrease" trend, as mentioned earlier:

When the propeller vertical offset Z_P increases from 0 to 30%R, the minimum spanwise lift of the wing drops while the maximum spanwise lift remains nearly unchanged. For both configurations, the maximum spanwise lift appears on the propeller upwash side, and the minimum value occurs on the downwash side.

As the propeller moves further downward to 120%R, the spanwise lift distribution changes dramatically. The peak spanwise lift shifts from the propeller upwash side to the vicinity of the propeller rotational axis, accompanied by a considerable increase in the minimum spanwise lift and substantially reduced spanwise lift fluctuations.

When the vertical offset of propeller is moved down from 120%R to 150%R, the lift enhancement near the upwash side of the second propeller from the root of wing is significantly weakened.

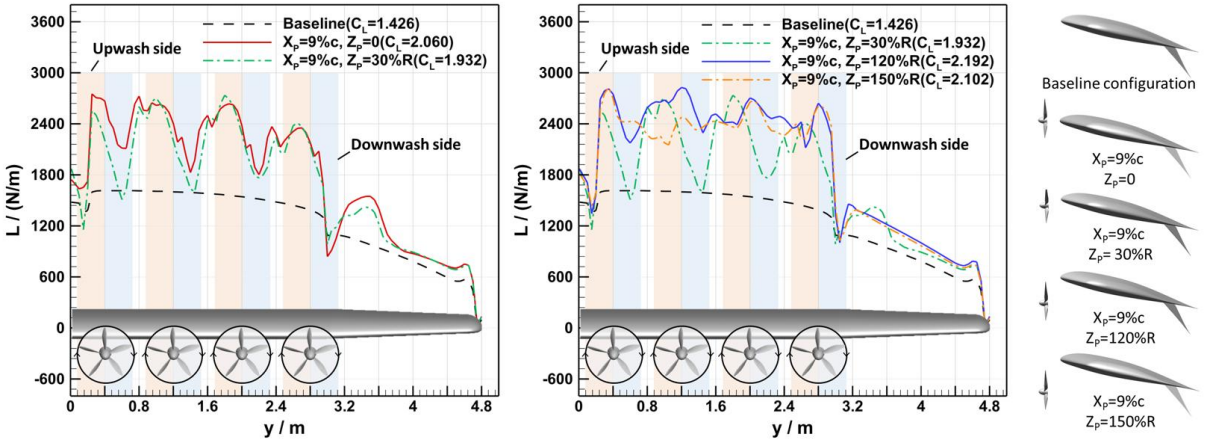
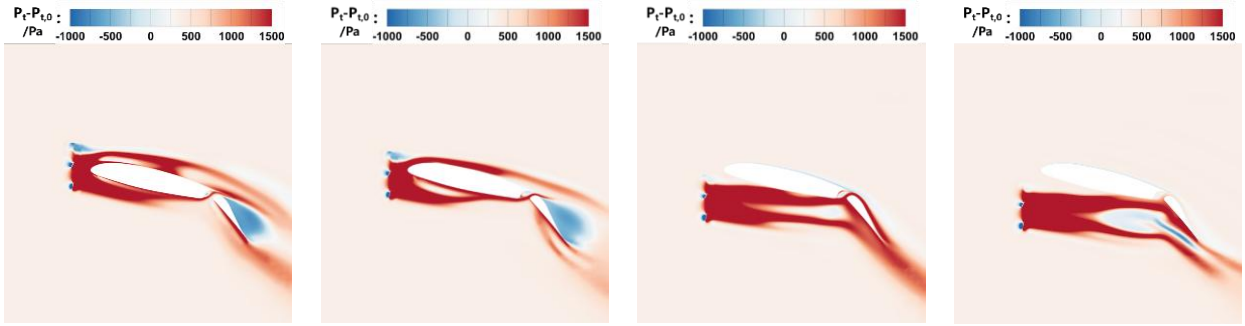


Figure 11 – Comparison of spanwise lift distribution under different propeller vertical offsets.

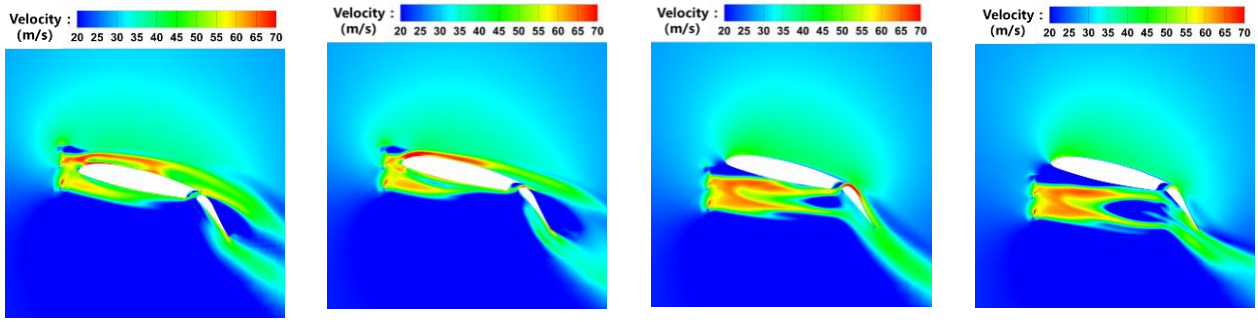
Taking section DV3 on the propeller downwash side, where local lift varies most obviously, as an example, the lift enhancement mechanism is analyzed. Figure 12 and Figure 13 present the total pressure and velocity distributions at section DV3 under different propeller vertical offsets, where P_t denotes total pressure and $P_{t,0}$ represents the total pressure of the far-field free stream.

It can be observed that the slipstream-affected region shifts downward along with the propeller, gradually shifting from the wing toward the flap. When the propeller moves downward from 0 to 30%R, the total pressure on the wing upper surface rises substantially, and part of the high-speed flow impinges on the wing surface. This reduces the pressure difference between the upper and lower surfaces and weakens the lift enhancement. As the vertical offset increases from 30%R to 120%R, the flow velocity over a certain area of the main wing lower surface decreases, which slightly enlarges the surface pressure difference. When the vertical propeller offset is 120%R, the slipstream effectively covers the flap upper surface and delays flow separation, thereby considerably increasing the lift contribution of the flap and improving the overall lift enhancement. When the vertical offset further increases from 120%R to 150%R, the slipstream exerts a weaker influence on the flap upper surface. Flow separation reappears on the flap, leading to another drop in lift enhancement.



(a) X_P=9%c, Z_P=0 (b) X_P=9%c, Z_P=30%R (c) X_P=9%c, Z_P=120%R (d) X_P=9%c, Z_P=150%R

Figure 12 – Total pressure distribution at DV3 under different vertical offsets.



(a) X_P=9%c, Z_P=0 (b) X_P=9%c, Z_P=30%R (c) X_P=9%c, Z_P=120%R (d) X_P=9%c, Z_P=150%R

Figure 13 – Velocity distribution at section DV3 under different vertical offsets.

Figure 14 further compares the pressure distributions at section DV3 under different vertical offsets. Compared with the propeller-free baseline configuration, the propeller slipstream reduces the peak

negative pressure at the leading edge of wing. The resulting lift loss limits lift enhancement on the main wing. In comparison, the flap exhibits a remarkable rise in lift enhancement. As discussed previously, at a vertical offset of 120%R, the favorable slipstream position maintains a satisfactory pressure distribution on the main wing and greatly increases the pressure difference between the upper and lower flap surfaces. Accordingly, the optimal lift enhancement is obtained at this vertical offset.

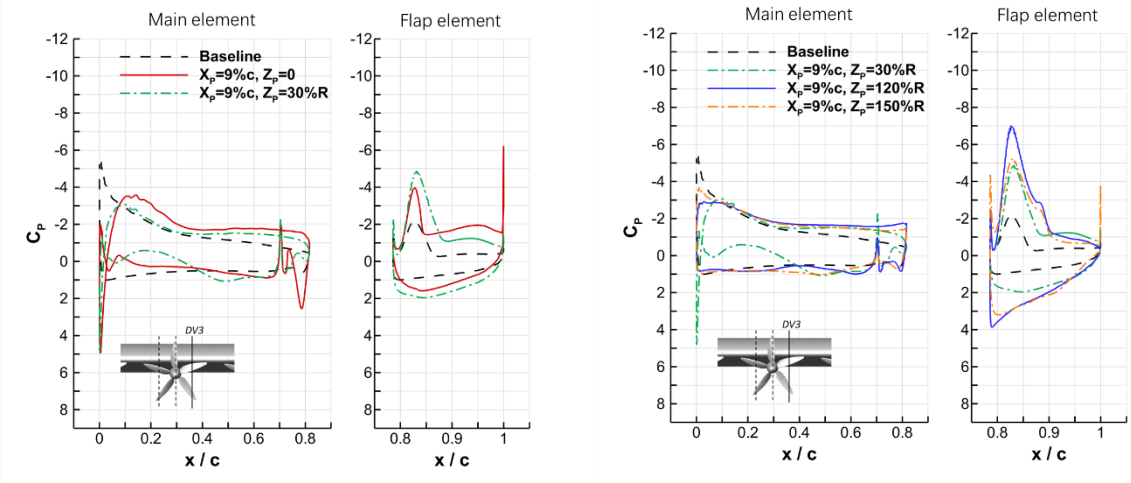


Figure 14 – Comparison of pressure distributions at section DV3.

4.2 Lift-Enhancement Mechanism Associated with Propeller Streamwise Offset

At 40° flap deflection and vertical offset Z_P=30%R, comparative analysis is performed on two typical configurations with streamwise offsets X_P=9%c and X_P=18%c.

Figure 15 compares the spanwise lift distributions of the baseline configuration and configurations with different propeller streamwise offsets at 40° flap deflection. Overall, changing the streamwise offset has only a limited effect on lift enhancement, with a lift coefficient difference of 0.064 between the two cases. In terms of spanwise distribution characteristics, both cases follow essentially the similar spanwise trends and exhibit periodic fluctuations corresponding to the propeller arrangement. Local lift peaks occur on the propeller upwash side, while local minima appear on the downwash side. This phenomenon can be explained as follows. On the upwash side, the propeller-induced velocity has an upward component, which considerably increases the local effective angle of attack and thus creates local lift maxima. On the downwash side, the downward induced velocity reduces the effective angle of attack, leading to local lift minima. These periodic fluctuations produce pronounced local non-uniformity in the spanwise lift distribution over the regions affected by the propeller slipstreams.

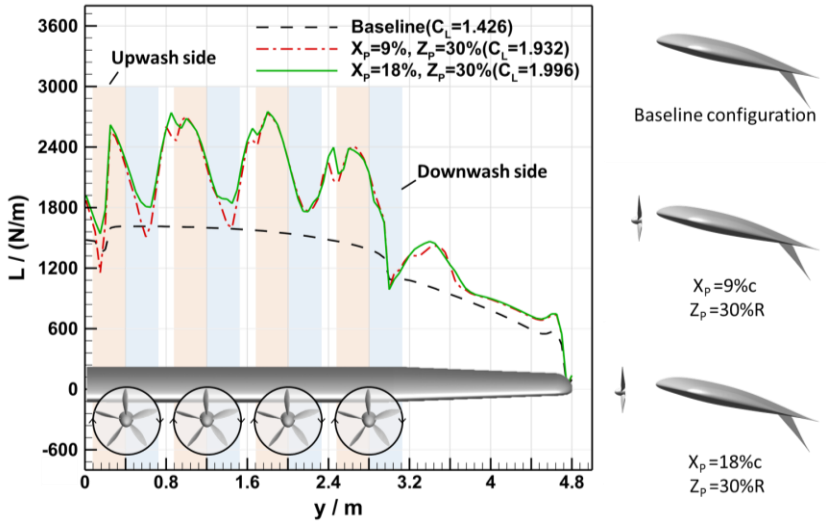
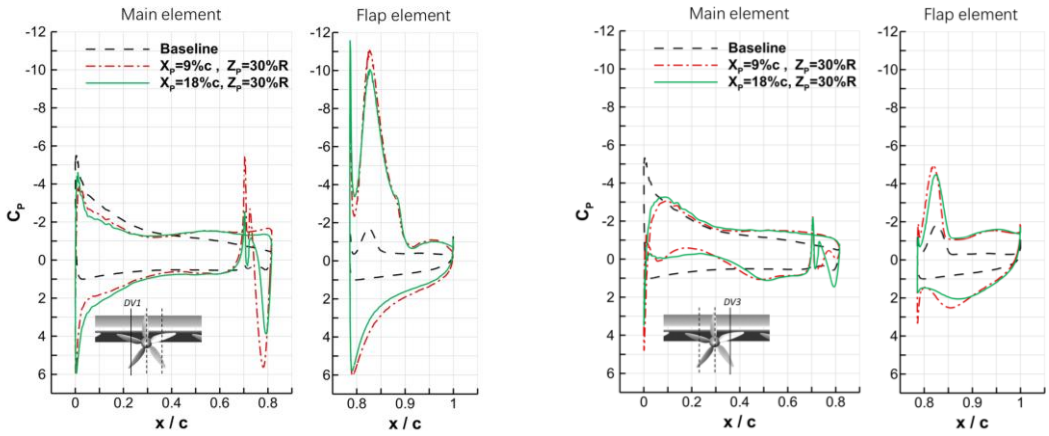


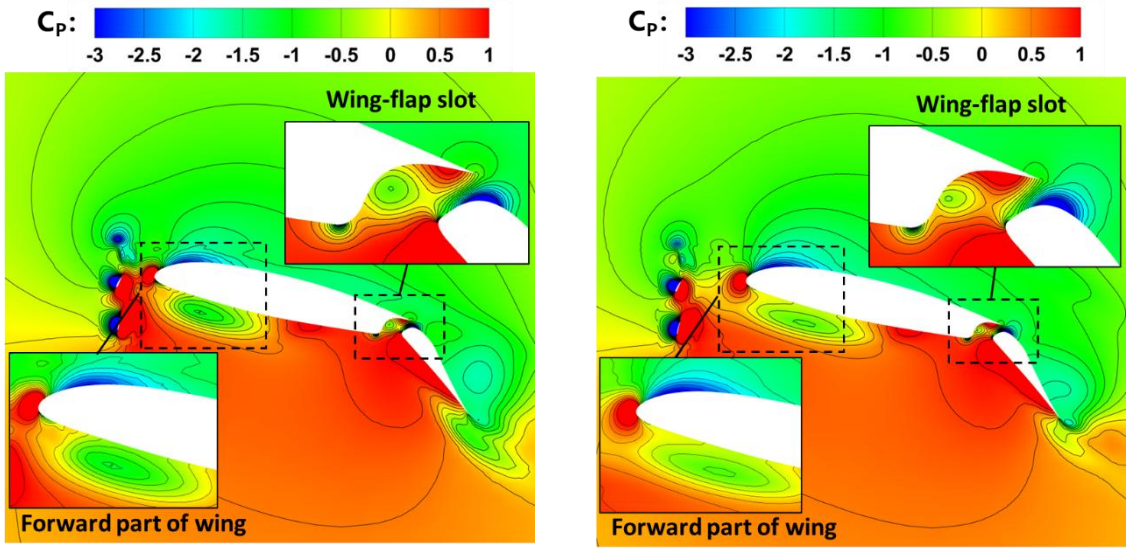
Figure 15 – Comparison of spanwise lift distribution under different propeller streamwise offsets.

When the propeller streamwise offset X_P increases from 9%c to 18%c, the local maximum lift remains nearly constant, while the local minimum lift increases slightly. To clarify the the underlying physical mechanism, the time-averaged pressure distributions at DV1 (upwash side) and DV3 (downwash side) are compared, as shown in Figure 16. The results show that the change in streamwise offset has a minor influence on the pressure distribution at DV1 on the upwash side, but exerts a more noticeable effect on DV3 on the downwash side. As illustrated in Figure 17, as the streamwise offset increases, the leading-edge suction region on the main-wing upper surface expands and the peak negative pressure on the upper surface increases. The shielding effect of the propeller hub on the main wing lower surface is evidently weakened, enabling effective pressure recovery on the lower surface and a slight rise in the pressure difference between the upper and lower wing surfaces. Meanwhile, the pressure near the wing trailing edge increases substantially, and the high-pressure area inside the slot expands accordingly, which further improves the overall lift performance.



(a) Section DV1 (b) Section DV3

Figure 16 – Comparison of surface pressure distributions at different sections.



(a) X_P=9%c, Z_P=30%R (b) X_P=18%c, Z_P=30%R

Figure 17 – Comparison of pressure distributions at section DV3 under different propeller streamwise offsets.

4.3 Lift-Enhancement Mechanism Associated with Propeller Tilt Angle

Figure 18 compares the spanwise lift distributions of the high-lift configuration at propeller tilt angles of 8° and 20°. The propeller positions and flap deflection are identical for both cases: X_P =9%c, Z_P =60%R and δ_f=40°. As the propeller tilt angle increases, the lift coefficient rises from 1.932 to 2.317. Both the local maximum and minimum values of the spanwise lift distribution increase, while their spanwise locations remain nearly unchanged.

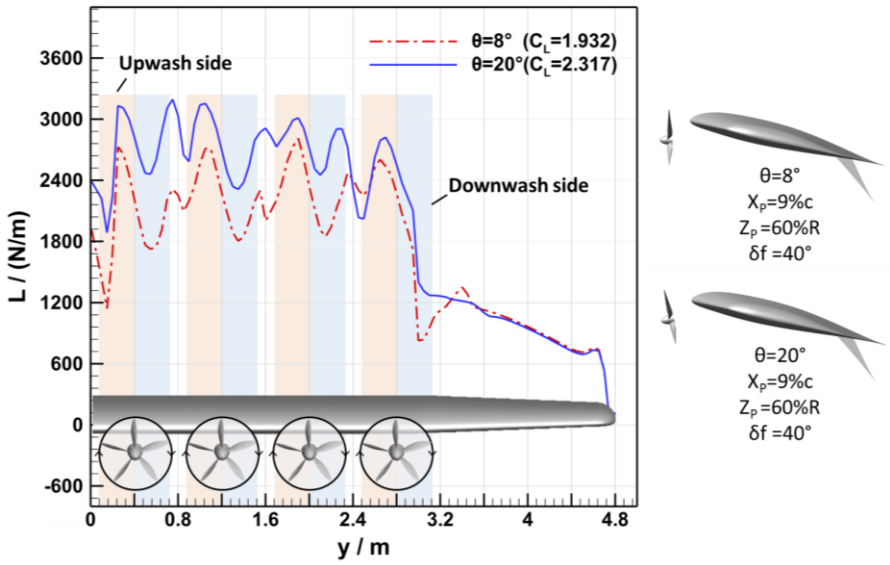
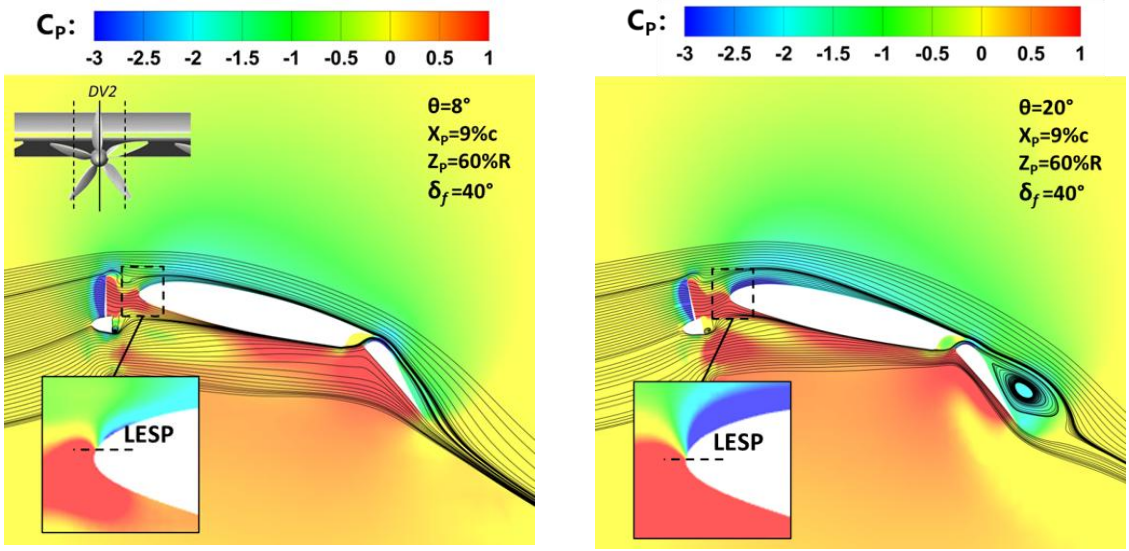


Figure 18 – Comparison of spanwise lift distribution under different propeller tilt angles.

The pressure distribution and streamlines at section DV2 (along the propeller central axis) are compared for tilt angles of 8° and 20°, as shown in Figure 19. As the propeller tilt angle increases, the slipstream is deflected more noticeably upward, and the velocity component normal to the wing is enhanced. This increases the local effective angle of attack at this section. Consequently, the leading-edge stagnation point moves toward the lower surface of the main wing, allowing more flow to pass over the upper surface. As a result, the leading-edge suction region expands, the suction peak increases, and the flow acceleration over the upper surface is strengthened. Meanwhile, the high-pressure region near the lower leading edge extends over a larger portion of the lower wing surface, further increasing the pressure difference between the upper and lower surfaces.

For the flap element, the upward deflection of the slipstream caused by the increased propeller tilt angle directs more airflow toward the main wing and reduces the flow impinging on the flap lower surface. The flow passing through the wing–flap slot is therefore weakened. Consequently, at a propeller tilt angle of 20°, the separated-flow region on the flap upper surface expands, and separation occurs farther upstream.



(a) Propeller tilt angle of 8° (b) Propeller tilt angle of 20°

Figure 19 – pressure distribution at section DV2 under different tilt angles

The pressure distribution at DV2 in Figure 20 further quantifies these variations. Compared with the tilt angle of 8°, the magnitude of the suction peak on the upper surface near the main-wing leading edge increases from approximately 3.4 to 6.2 at a tilt angle of 20°, representing an increase of 82%. Although the pressure peak on the lower surface near the leading edge decreases from about 5.4 to

4.5, the overall pressure difference between the upper and lower surfaces of the main wing increases markedly because of the expansion of the high-pressure region on the lower surface and the strengthened suction on the upper surface.

For the flap, the flow separation point on its upper surface moves forward from x/c≈0.9 to around x/c≈0.85 as the tilt angle increases to 20°. Nevertheless, the lift gain of the main wing is substantially larger than the lift loss associated with the increased flap separation. Therefore, the total lift at this section is significantly improved.

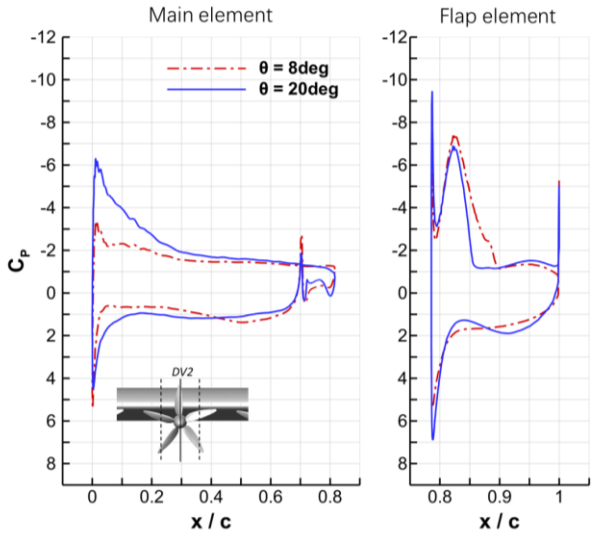


Figure 20 – Comparison of surface pressure distributions at DV2 under different tilt angles.

5. Conclusion

This study investigates the effects of propeller vertical offset Z_P, streamwise offset X_P, and tilt angle θ on the lift-enhancement characteristics of a high-lift configuration under takeoff conditions using a momentum source RANS method. High-fidelity URANS simulations are further conducted for representative configurations to reveal the mechanisms of slipstream-induced lift enhancement. The main conclusions are as follows:

(1) The propeller vertical offset has a significant influence on lift enhancement. At a flap deflection angle of 40° and a streamwise offset of 9% of the mean aerodynamic chord, the lift enhancement first decreases, then increases, and finally decreases as the vertical offset increases. When the vertical offset reaches 120% of the propeller radius, the maximum increase in lift reaches 53.7% relative to the baseline configuration without propellers.

(2) Increasing the vertical offset moves the propeller slipstream downward, shifting the slipstream-affected region from the main wing toward the flap. At an appropriate vertical offset, the slipstream effectively covers the flap surface and significantly suppresses flow separation over the flap upper surface, thereby enhancing the lift contribution of the flap. Meanwhile, adjusting the vertical offset also improves the uniformity of the spanwise lift distribution.

(3) The lift enhancement effect of slipstream shows no obvious variation with propeller streamwise offset. With the vertical offset fixed at 120% of the propeller radius, increasing the streamwise offset to 13.5% of the mean aerodynamic chord improves the lift enhancement to 54.1%. However, increasing the streamwise offset has only a limited effect on the spanwise lift distribution, with the local maximum remaining nearly unchanged and the local minimum increasing slightly.

(4) An appropriate increase in propeller tilt angle can further improve the lift enhancement of the configuration. Increasing the tilt angle deflects the slipstream upward, moves the leading-edge stagnation point downward, and increases the effective angle of attack. As a result, both the local maximum and minimum values of the spanwise lift distribution are increased, improving the lift characteristics of the high-lift configuration.

Future work will focus on the integrated optimization of propeller-position parameters and flap geometry to further improve the lift-enhancement capability. In addition, the noise characteristics associated with propeller slipstream–flap-slot interaction will be investigated.

6. Acknowledgments

This work was supported by the National Key Research and Development Program of China under Grant No. 2023YFB3002800, and the numerical calculations in this paper were performed using the Xi'an Advanced Computing Center.

7. Contact Author Email Address

Wen-Ping Song, Professor, wpsong@nwpu.edu.cn, corresponding author.

8. Copyright Statement

The authors confirm that they, and/or their company or organization, hold copyright on all of the original material included in this paper. The authors also confirm that they have obtained permission, from the copyright holder of any third-party material included in this paper, to publish it as part of their paper. The authors confirm that they give permission or have obtained permission from the copyright holder of this paper, for the publication and distribution of this paper as part of the ICAS proceedings or as individual off-prints from the proceedings.

References

[1] Courtin C and Hansman R J. Safety considerations in emerging electric aircraft architectures. *18th AIAA Aviation Technology*, Integration, and Operations Conference, Atlanta, Georgia, pp 1-17, 2018.

[2] Kim H D, Brown G V and Felder J L. Distributed turboelectric propulsion for hybrid wing body aircraft. *2008 International Powered Lift Conference*, London, United Kingdom, pp 1-8, 2008.

[3] Veldhuis L L M. Review of propeller-wing aerodynamic interference. *24th International Conference of the Aeronautical Sciences*, Edinburgh, United Kingdom, Vol. 6, No. 1, pp 2004-2006,2004.

[4] Cheng Z Y, Yang Y X and Ye B. Parameterization investigation on distributed electric propulsion aircraft aerodynamic characteristics. *Journal of Physics: Conference Series*, Vol. 2459, No. 1, pp 012092, 2023.

[5] Seo Y, Hong Y and Yee K. Numerical investigation of wing–multiple propeller aerodynamic interaction using actuator disk method. *International Journal of Aeronautical and Space Sciences*, Vol. 23, No. 5, pp 805-822, 2022.

[6] Chen S Q, Guo Z and Liu D N. Impact of propeller arrangement on aerodynamic performance for a high-lift distributed propulsion system. *Engineering Applications of Computational Fluid Mechanics*, Vol. 19, No. 1, pp 2505701, 2025.

[7] Aref P, Ghoreyshi M, Jirasek A, Satchell M J and Bergeron K. Computational study of propeller-wing aerodynamic interaction. *Aerospace*, Vol. 5, No. 3, pp 79, 2018.

[8] Keller D. Towards higher aerodynamic efficiency of propeller-driven aircraft with distributed propulsion. *CEAS Aeronautical Journal*, Vol. 12, No. 4, pp 777–791, 2021.

[9] Cao M Z, Liu K, Wang C Q, Wei J B and Qin Z J. Research on the distributed propeller slipstream effect of uav wing based on the actuator disk method. *Drones*, Vol. 7, No. 9, pp 566, 2023.

[10] Keller D. Numerical study on lift augmentation via distributed propulsion for a propeller driven regional transport aircraft in landing configuration. *CEAS Aeronautical Journal*, Vol. 17, pp 553-566, 2026.

[11] Firnhaber Beckers M, Schollenberger M, Lutz T, Bongen D, Radespiel R, Florenciano J L and Funes-Sebastian D E. Numerical investigation of high-lift propeller positions for a distributed propulsion system. *Journal of Aircraft*, Vol. 60, No. 4, pp 995-1006, 2023.

[12] Li J Y, Cui W, Wang Q M and Wu D. Aerodynamic design of distributed propulsion with slipstream effects in double-slotted flap configurations. *Acta Aeronautica et Astronautica Sinica*, Vol. 47, No. 7, pp 633240, 2026.

[13] Agrawal D, As'ad F, Berk B, Long T, Lubin J, Courtin C, Thomas J, Hansman R and Drela M. Wind tunnel testing of a blown flap wing. *AIAA Aviation 2019 Forum*, Dallas, Texas, pp 1-20, 2019.

[14] Fei X, German B J and Patterson M D. Exploring the effects of installation geometry in high-lift propeller systems. *2018 AIAA Aerospace Sciences Meeting*, Florida, USA, 2018.

[15] Spalart P R and Allmaras S R. A one-equation turbulence model for aerodynamic flows. *30th aerospace sciences meeting and exhibit*, Nevada, USA, pp 439, 1992.

[16] Hough G and Ordway D. The generalized actuator disk. *Second Southeastern Conference on Theoretical and Applied Mechanics*, pp 1-36, 1964.

[17] Reissner H. On the vortex theory of the screw propeller. *Journal of the Aeronautical Sciences*, Vol. 5, No. 1, pp 1-7, 1937.

[18] Sinnige T, Arnhem N V, Stokkermans T C A, Eitelberg G, and Veldhuis L L M, Wingtip-mounted propellers: aerodynamic analysis of interaction effects and comparison with conventional layout. *Journal of Aircraft*, Vol. 56, No. 1, pp 295–312, 2019.